

**Induced Microearthquake Patterns and Oil-Producing
Fracture Systems in the Austin Chalk**

W. S. Phillips, Nambe Geophysical, Inc.

T. D. Fairbanks, Nambe Geophysical, Inc.

J. T. Rutledge, Nambe Geophysical, Inc.

D. W. Anderson, Los Alamos National Laboratory

Submitted to *Tectonophysics*

Special Issue on Induced Seismicity

LAUR 96-3834

Abstract

Microearthquakes collected during hydraulic stimulation allowed us to study fracture zones in Austin chalk oil reservoirs at two sites in the Giddings field, Texas. We deployed three-component, downhole geophone tools in production wells at depths of 2100 m and greater, one near Cook's Point, and two on the Matcek lease near Caldwell. At Cook's Point, we collected 482 microseismic events during a 4000 m³ (25,000 bbl) hydraulic stimulation in an offset well. We collected 770 events during a similar operation on the Matcek lease. Many seismograms contained reflected phases that constrained location depths to the production zone at the base of the Austin chalk. By restricting all microearthquake locations to production depths, we located 20% of the Cook's Point events and over 60% of the Matcek events. At both sites we observed only the fracture wing closest to the observation stations. Locations formed elongated patterns extending up to 1 km from the stimulation well and trending N60°E, parallel to the known, regional fracture trend. The Cook's Point seismic zone measured over 100 m in width, while long stretches of the Matcek seismic zone narrowed to 30 m or less. We believe the width of the seismic zone reflected the density of conductive fractures and thus, the volume of the reservoir accessed by the stimulation. Indeed, production rates in the first year following stimulation were much higher at Cook's Point, where we observed the wider of the two seismic zones.

Introduction

Hydraulic stimulation is an effective technique that has found widespread use in enhancing production from oil and gas fields. In the fractured, but otherwise low-permeability Austin chalk of the Giddings field, Texas, hydraulic stimulation is routinely applied to force water into untapped reservoir areas. In addition to creating new flow paths, the water is thought to dislodge hydrocarbons residing in small cracks through a capillary process (imbibition) and the hydrocarbons become more mobile and easily produced. Other than their general orientation, little is known about the fracture systems that are affected by the stimulations and that define reservoir extent and profitability in the Giddings field.

Downhole microseismic monitoring has been used to study the fracture systems affected by hydraulic stimulation in hot-dry-rock geothermal reservoirs in the U.S. (Pearson, 1981; House, 1987; Fehler et al., 1987; Fehler and Phillips, 1991), the U.K. (Batchelor et al., 1983; Baria and Green, 1986), Japan (Niitsuma et al., 1987) and France (Cornet and Scotti, 1993). The data are of high enough quality to allow tomographic imaging of the fractured volume (Block et al., 1994) and the mapping of individual slipping joints on scales as small as 40 m (Roff et al., 1996; Phillips et al., 1997). These experiments have taken place in hard-rock environments, mostly crystalline, through which elastic waves propagate efficiently. However, hydrocarbon reservoirs are generally found in sedimentary environments where elastic waves propagate less efficiently. Despite this, induced microearthquakes have been successfully mapped in sedimentary environments, often by

employing close-in wells that are expressly drilled for instrumentation purposes (e.g. Vinegar et al., 1991; Keck and Withers, 1994; Warpinski et al., 1996).

In the following, we will describe downhole, microseismic monitoring of hydraulic stimulations of the Austin chalk in the Giddings field, Texas (Figure 1). We deployed geophones in existing production wells to test whether or not high-quality data could be acquired in the Giddings without the expense of drilling instrumentation wells. Given the necessarily limited sensor geometry, we had to include P-wave particle-motion (hodogram) and reflected phase data to locate microearthquakes. To calibrate the experiment sites, we combined hodogram and arrival-time data in a joint, hypocenter-velocity inversion. Because the use of hodogram data is unusual in such calculations, we include a description of the method.

These deployments were intended as reconnaissance experiments, to test levels of seismic activity before deploying more extensive station arrays. However, the data were of such quality to allow accurate mapping of the microearthquakes and to find a positive correlation between the lateral extent of the seismic zones and post-stimulation, oil-production rates.

Setting

Cumulative oil production from the Giddings field, Texas, has reached 60 million m^3 (380 million bbl) of oil and 60 billion m^3 (2.1 trillion cubic feet) of gas, nearly all from the Austin chalk. The Austin chalk is a fractured limestone with a matrix porosity of 5-8% and matrix permeability of 0.01 to 0.1 millidarcys. The fractures resulted

from the bending of the brittle Austin chalk over a deeper and older Jurassic shelf margin, and trend N60°E, roughly parallel to the Gulf coast (Figure 1). Producing fractures are vertically oriented and are more easily encountered by drilling horizontal wells.

Horizontal drilling has increased dramatically; however, the identification of fractures is still key to the success of any well in the Austin chalk. The ability to determine the location and direction of these fractures and their lateral and vertical extent would allow increased efficiency for draining this reservoir. Recovery efficiency from the Austin chalk in the Giddings field is thought to be on the order of 7-10% of the original oil in place. In addition to helping with efficient well placement for primary production, fracture maps will be crucial for planning any future, enhanced recovery processes.

Data

Data Acquisition. We deployed downhole geophones within and just above the producing (Ector) member of the Austin chalk at two sites in the Giddings field (Figure 1). At Cook's Point we occupied Exxon well CPU 1-2 from 9/91 to 11/91. On the Matcek lease near Caldwell we occupied Exxon wells Matcek 4 from 11/91 to 9/92 and Matcek 3 from 5/92 to 9/92. To protect tools during their extended time downhole, and to reduce noise, the monitor wells were plugged above the reservoir perforation interval and filled with anticorrosive liquid. Three-component geophone tools were placed 5-10 m above the plugs and secured with a single locking arm. Geophone depths were 2100 m at Cook's Point and nearly 2300 m at the Matcek site. We used critically-damped, 8-Hz geophones, with downhole amplification. A 1-

KHz lowpass filter was applied uphole before digitizing at 5 KHz. An event detector operated on the digitized stream (Lee et al., 1989), storing signals on disk for later analysis.

Association of Microearthquakes with Pressurization. In over a year of monitoring in the Giddings field, the only microearthquakes we recorded were induced by pressurization. During the hydraulic stimulation of well CPU 2-2, we collected 482 microseismic events that contained clear compressional (P) and shear (S) phases, resembling tectonic microearthquakes. Later, we collected 770 events during the stimulation of the Matcek 1. A few events were collected during a stimulation of the more distant Matcek 2 and at the time of a flange failure in a nearby horizontal well (Matcek 6H) that introduced water to the formation under hydrostatic head and caused a small, unplanned hydraulic fracture. No other microearthquakes were recorded during our monitoring period.

At the Cook's Point and Matcek sites, the first microearthquakes were observed within one hour of the beginning of pumping (Figure 2). Event rates peaked at 4 and 7 per minute, respectively, and decayed away after final shut-in. Maximum pumping rates were $13 \text{ m}^3/\text{s}$ and well-head pressures reached 21 MPa. Low-pressure intervals indicate the addition of rock salt, followed by an acid gel, to the injected fluid. This is done to plug previously drained fractures and encourage stimulation fluids to move into untapped regions of the reservoir. At Cook's Point, peaks in seismic activity followed the addition of rock salt and acid by roughly 30 minutes. On the Matcek lease, peak activity coincided with the low-pressure, rock salt-acid pumping intervals. Small peaks were associated with final shut-in at both sites.

Microearthquake Data. A sample microearthquake seismogram is shown in Figure 3. The horizontal components have been rotated so that the P-wave amplitude is maximized on the radial and minimized on the transverse components, following Flinn (1965). The product of radial and vertical components is also shown in Figure 3. For inclined raypaths, the product signal should be of opposite sign for P and vertically polarized shear (SV) phases.

We observed compressional and dilatational first motions, and high S-to-P amplitude ratios, both typical of tectonic earthquakes. This indicates failure mechanisms with a large component of shear slip, consistent with previous hydraulic stimulation studies (e.g. Albright and Pearson, 1982).

Microearthquake signals recorded above the Ector layer (Cook's Point and Matcek 4 geophones) peaked in the 200-400 Hz band (Figure 4). Because signals recorded at the Matcek-3 geophone, located in the Ector layer, contained higher frequencies (good signal-to-noise ratio up to 500 Hz), attenuation along the path above the Ector may have affected the waveforms. Some of the peaking may be a coupling effect, between the geophone tool and the well casing, or between the casing and the surrounding rock.

We observed secondary phases following the S waves in many vertical- and radial-component seismograms, especially for more distant events, at both sites (Figure 3). Considering relative arrival times and the SV motion at the geophone, these phases appear to be SV-to-SV reflections off the high-contrast interface (sonic log P-wave velocities of 3.21 and 5.54 km/s) between the Eagleford and Buda

formations, below the Austin chalk (see Figure 1). For this high-contrast interface, total internal reflection of SV waves occurs for angles of incidence greater than 37° (using SV velocities found during calibration), or for distances greater than 210 m (Cook's Point), 220 m (M3), or 240 m (M4), assuming the events occurred at stimulation depths. We matched the relative arrival times and amplitudes of the reflections with synthetic data, calculated using a reflectivity code (Randall, 1994), for event depths within the Austin chalk (Figure 5). The synthetic seismograms were calculated using a double-couple source, oriented to roughly match major features of the seismic data in Figure 3. As we will show later, the reflections become important in constraining microearthquake depths.

Horizontally polarized shear waves (SH) arrived before the SV waves, indicating significant anisotropy within the reservoir. Arrival-time differences (SV-SH) increased linearly with SV-P time (Figure 6), or distance, and showed little dependence on propagation azimuth (Figure 7). This indicates the anisotropy arises from horizontally, rather than vertically aligned structure, perhaps fine-scale bedding. We investigate anisotropic effects no further in this paper. However, we consider polarization when determining S-wave arrival times to avoid using a mixture of SV and SH times to locate events.

Perforation-Shot Data. Perforation shots were fired in the stimulation wells at reservoir depths to prepare for the hydraulic stimulations and we used the seismic data they generated to help calibrate the experiment site. The first shot at Cook's Point was not observed seismically, but the treatment well was found to be dry, suggesting that the shot energy was lost to the air column. Water was

added prior to subsequent shots to increase the tamping effect. Signals were then observed easily at ranges up to 700 m (Figure 8). We were unsuccessful in recording zero times for shots in wells CPU 2-2 and Matcek 1, the injection wells for the two experiments described here.

Perforation-shot waveforms were different from those of microearthquakes, which can be attributed to the difference in source type. The 6.1 m (20 ft) perforation tool contained 20 shaped charges of 10 g each, distributed in a spiral pattern around 6.7 m (22 ft) of primacord. The shots produced strong P waves, as well as P-to-P and P-to-SV reflections off the Eagleford-Buda interface. We observed strong, direct SH but poor SV arrivals. The SH energy may have been generated by shape charges pointing in directions transverse to the ray path. Figure 8 shows a weak arrival on the radial component, just prior to the SH arrival. If this is direct SV it is our only observation of SV arriving before SH. For a later shot at the Matcek site, we observed a weak SV phase that followed SH. From a simple borehole shot, we expect P radiation to be strong in horizontal directions, but not SV (Fehler and Pearson, 1984), consistent with our perforation-shot P and SV observations.

Data Reduction Prior to Location. Because deployments consisted of, at most, two downhole stations, we had to use P-wave hodogram orientations in addition to arrival times to locate microearthquakes. In isotropic media, the P-wave orientation points along the arriving raypath, so we can use hodogram data to constrain the microearthquake location. In our case, anisotropy with a vertical symmetry axis may bias angles of incidence calculated from hodograms, yet allow propagation azimuths to be obtained reliably.

We employed eigenvector analysis (Flinn, 1965) to compute hodogram orientations using the first cycle of the P wave. Hodogram inclinations (from vertical) were calculated using all three components of motion and hodogram azimuths were calculated using the two horizontal components. Hodogram linearity (Vidale, 1986) was used as an estimate of the quality of the hodogram measurement. Linearity ranges from zero (spherical motion) to one (linear motion).

We then determined arrival times manually after rotating horizontal-component seismograms to radial and tangential components based on P-wave hodogram azimuths (Figure 3). A subjective quality value was assigned to each arrival time. High-quality SV was slightly more plentiful than SH for the microearthquakes, so we used the SV data to obtain locations. We judged hodogram azimuth errors to be 5° to 10° and arrival time errors to be 1 ms, 2 ms and 5 ms for P, SV and reflected phases, respectively.

We found it difficult to constrain microearthquake depths using the hodogram inclination data. High-quality (linearity > 0.8) inclination data are plotted versus the SV-P time in Figure 9. We also show where the inclinations should fall if events occurred within the producing interval (Ector member) of the Austin chalk. Inclinations measured from Matcek 4 and CPU 1-2 geophones were steep, indicating events occurred below the Austin chalk, in the Eagleford shale. This is a surprising result because the Eagleford is more ductile and contains far fewer fractures than the chalk. Inclinations from the Matcek 3 geophone indicated nearby events occurred over a range of depths within the Ector layer, but more distant events occurred above the Ector. In addition to these conflicting and unrealistic trends, we

observed considerable scatter in the inclination measurements. Because small changes in angle of incidence at the sensor result in large changes in location depth for these high-contrast velocity structures, any scatter will be magnified in the event locations. Because of these problems, we discarded the inclination data and decided to use reflected phases to provide depth control in the location calculations.

Calibration and Location Methods

In the Austin chalk, calibration consisted of estimating geophone orientations and P and SV velocities in important layers. We used well-log and perforation-shot data to obtain an initial model. Then we applied a joint hypocenter-velocity inversion that included hodogram azimuth data to refine the calibration.

Initial Calibration. We started by orienting the geophones using P-wave hodograms from the perforation shot. To construct a velocity model, we obtained depths to geological interfaces using resistivity-log data taken in monitor and injection wells. Horizontally layered models described the structure well at both sites (interface gradients were 1% or less between wells). We estimated the P-wave velocity of the Ector member of the Austin chalk from sonic logs taken in the Cook's Point area (4.70 km/s) and using perforation-shot data from the Matcek-2 well, recorded at the Matcek-4 geophone, where we successfully recorded a zero time (4.75 km/s). SV velocity in the Austin chalk could then be estimated using perforation-shot, SH-P times (e.g. Figure 8) after adjusting for the expected shear-wave splitting (Figure 6), obtaining 2.35 km/s. We set SV velocities in other layers using the P/SV velocity ratio found for the Austin chalk, Ector layer.

Joint Hypocenter-Velocity Inversion. We refined the initial velocity model and geophone orientation estimates using a layered model, joint hypocenter-velocity inversion, performed using a subset of events with high-quality, arrival-time and hodogram azimuth data. The inversion adjusts any combination of velocities, station time corrections and geophone orientations along with the event locations to fit the arrival-time and hodogram data in an iterative, damped, least-squares procedure. To avoid unresolvable combinations of unknown parameters, we checked for singularity before damping was applied. Time and angular units were scaled to be of similar magnitude to avoid numerical problems in forming the normal equations. Data were weighted by our estimates of uncertainty, scaled as above. We employed the parameter-separation technique (Pavlis and Booker, 1980) which decouples model parameter and event location solutions, allowing large numbers of events to be included.

We treated velocities as isotropic. Because the anisotropy symmetry axis is oriented vertically, velocities should be independent of propagation azimuth. Thus, for ray paths of similar angles of incidence (nearly horizontal for events at producing depths), an isotropic velocity model is sufficient.

We calculated event locations using the standard, Geiger's method, modified to include hodogram data and employing unit scaling and error weighting as described above. Because hodograms only indicate raypath orientation, not propagation direction, for each iteration we chose the direction that fit the current location the best. Finally, certain combinations of data, such as one P, one SV and one 3-dimensional hodogram orientation, yield several distinct, but equally possible

solutions. We used a grid of initial locations to capture all solutions, discarding local minima. If a well-constrained location pattern had been established, we chose the location that aligned the best. If not, we used independent information (known fracture-system orientation) to choose between locations.

Results

We only used microearthquakes that produced reflected arrivals in the joint hypocenter-velocity calibration procedure. Location depths were constrained well by the reflection data and fell in the expected production depth interval. Based on this, we fixed depth and proceeded to locate as many microearthquakes as possible, including those without reflected arrivals. In the following, we describe the results of the calibration and the fixed depth location procedures.

Joint Hypocenter-Velocity Calibration. We calibrated the Matcek field area using 51 high-quality events containing two P, two SV and one or more reflected arrivals, as well as one or more hodogram azimuths of linearity greater than 0.8, recorded by the two-geophone array during stimulation of the Matcek 1. We fixed the Austin chalk P-wave velocity to 4.75 based on results from the perforation shot with a successfully recorded zero time. We chose the shot result rather than a sonic log velocity because the shot raypath was more representative of microearthquake raypaths. We solved for SV velocities in the Austin chalk and Eagleford layers and geophone orientations in the Matcek 3 and 4 wells. SV velocity remained at 2.35 ± 0.1 km/s in the Austin chalk (Ector) and moved to 1.78 ± 0.2 km/s in the Eagleford. Geophone orientations rotated $5 \pm 1^\circ$ from our initial guess (based on perforation-

shot hodograms) at the Matcek 4 and $12 \pm 2^\circ$ at the Matcek 3. The quoted errors represent the standard errors of the solution, using our initial errors as estimates of the data variance. The inversion reduced RMS P and SV arrival-time residuals by less than 20% to 1.0 and 1.8 ms, respectively, and reduced the RMS azimuth residuals by 50% to 8° and 12° at the Matcek 4 and 3, respectively. These RMS residuals are similar to our initial data-error estimates. The velocity results are slightly, but not substantively, different from results of a joint-hypocenter-velocity inversion applied to arrival times only, quoted in Phillips et al, 1996.

Location depths of the 51 calibration microearthquakes were constrained well by the reflection data (Figure 10). Most events fell within 20 m of the base of the Austin chalk where the injection took place, demonstrating a dramatic improvement from what could be obtained using hodogram inclinations. From Figure 9, hodograms indicated considerable scatter in location depths, ranging well above and below the producing zone. In map view, locations defined a narrow, linear trend (Figure 10), parallel to the known fracture trend in the Giddings field (Figure 1).

We also located Cook's Point events that contained high-quality P, SV and reflected phases and a hodogram azimuth of linearity 0.8, using the velocities obtained above. Location depths scattered more than at the Matcek site, but still clustered around the base of the Austin chalk (Figure 11).

Fixed-Depth Locations. To locate a larger number of microearthquakes, we fixed event depth to the middle of the production interval near the base of the Austin chalk. The narrow depth range

found for high-quality events during calibration justified this step. This allowed the location of 490 Matcek-1 events (60% of the total) that contained three or more, high- and mid-quality, direct-wave arrivals (Figure 12). We used azimuth data if hodogram linearity was greater than 0.5.

The new location pattern fell along the trend found during the calibration of the Matcek site and extended 1 km from the stimulation well. Events located near the injection well were over 700 m from the M3 geophone. Because the tip of the seismic zone fell only 500 m, at most, from the M3 geophone, we believe the full length of the wing of the stimulation was visible. The seismic zone was less than 30 m wide over much of its length. The widest section of the seismic zone fell between the two stations where we find the largest location errors.

For the single-station experiment at Cook's Point, we based locations on P and SV arrival times and a hodogram azimuth, of linearity greater than 0.8. Location depth was fixed as above. Only 96 events (20% of total) generated P waves strong enough to provide high-quality hodogram azimuths. Under these criteria, the most distant locatable events fell just over 400 m from the monitor station (Figure 12). Thus, only a portion of one wing of the stimulation was visible. The width of the seismic zone was greater than 100 m over most of the observable length. The width was constrained well by P and SV arrival times as reflected in the error ellipses.

The seismic zones were active along most of their lengths throughout the stimulation. Events occurred at the outermost edges within one hour of the first observed events at both sites. In addition to

some small-scale, space-time clustering, the most anomalous behavior was a set of events that occurred late, after shut-in, near the injection well at the Matcek site.

Discussion

The distribution of stimulation-induced microearthquakes indicates the extent of the reservoir that is hydraulically connected and has been raised to a pressure level sufficient to cause slip. Stimulation fluids may have penetrated into a slightly larger volume of the reservoir than is defined by the seismicity, but the two volumes should be of similar shape. In the Austin chalk, hydraulic stimulation is intended to create new flow paths and mobilize oil in small cracks through imbibition. Therefore, the effectiveness of the stimulation in producing more oil should be related to the volume of the associated seismic zone.

We observed two hydraulic stimulations in the Austin chalk. Both seismic zones are similarly oriented, trending N60°E, parallel to the trend of the regional folding responsible for the major fracture system. However, the Cook's Point seismic zone is wider than the Matcek zone. This indicates a larger reservoir volume may have been affected by the stimulation, perhaps related to a higher population of fractures at Cook's Point. Production records show a much larger increase in oil rate from the Cook's Point well following stimulation (Figure 13). The correlation between seismic zone width and production suggests that hydraulic stimulation microseismicity is relevant to oil production in the Austin chalk and merits further investigation. To more fully understand fracture systems and the potential of microseismic

techniques, the results should be compared to independent measurements of fracture density, such as can be obtained from estimates of anisotropy from surface seismic data (Mueller, 1992).

We investigated whether or not the difference in seismic zone widths could result from larger errors for the Cook's Point, single-station experiment. To convince ourselves, locations were obtained using data from the Matcek 3 and 4 stations independently (Figure 14). Both results show narrow seismic zones over the 200-300 m length of the fracture closest to each station, while some scatter occurs at greater distance where raypath azimuth errors may be large. At Cook's Point, we see a broader seismic zone over the 200-300 m closest to the station.

We also considered how our assumption of a fixed depth might affect location patterns if events were actually distributed throughout the Austin chalk (Ector) interval. To do this, we synthesized data for the Cook's Point geometry, placing events over the entire Ector depth range on a vertical plane striking N60°E. After fixing depth as above, locations spread only 10 m from the test plane.

In addition to the seismic zone widths, we see other indications that fracture density might be different between the two sites. Because more distant events are locatable, even for the single-station calculations (Figure 14), the seismic Q of the Austin chalk may be higher at the Matcek site. Unless events are systematically larger, waves propagate more efficiently there, consistent with a lower density of fractures. We can not confirm this with observations of shear-wave splitting that might indicate different populations of aligned, sub-

vertically oriented fractures. Azimuthal variations in shear-wave splitting were not apparent at either site.

The microseismic monitoring experiments we have done in the Austin chalk were relatively inexpensive because downhole instruments were deployed in existing wells. However, the deployments incurred costs through the rig time needed to pull tubing and set bridge plugs and through the lost revenue while the monitor wells were off-line. If microseismic studies are to be run routinely in the Giddings field, these expenses will have to be minimized. One development that will eliminate rig expenses and limit well down time to a few days is a monitoring device slim enough to pass through the production tubing.

Conclusions

Fractures are pervasive in the oil-bearing Austin Chalk of the Giddings field, Texas, and result from the bending of the brittle limestone over a Jurassic-age shelf margin. The success of an oil well in the Austin chalk depends on intersecting fractures that allow connection with a large volume of the reservoir. We deployed downhole geophone tools at depths over 2100 m at two sites in the Giddings field, Texas, to study microseismicity related to hydraulic stimulation of the Austin chalk that might lead to greater understanding of the fracture system. We summarize our results and conclusions as follows.

1. For two monitoring periods totaling one year, the only microseismicity we observed was associated with reservoir pressurization. During routine 4000 m³ (25,000 bbl) hydraulic stimulations, we recorded 482 shear-slip events using one station at Cook's Point and 770 using two stations on the Matcek lease near

Caldwell.

2. Microearthquakes appeared to be shear-slip events, consistent with previous studies of hydraulic stimulation microseismicity.

3. We observed strong anisotropic effects, likely related to fine-scale bedding, that had to be considered during data reduction and location phases of the study.

4. Hodogram azimuth data proved indispensable in locating microearthquakes. However, hodogram inclinations gave inconsistent and unrealistic estimates of microearthquake location, especially depths.

5. We observed secondary waves in many seismograms. These were attributed to SV-to-SV reflection off of a high-contrast interface below the Austin chalk, and were used to constrain location depths.

6. A joint hypocenter-velocity inversion that incorporated hodogram azimuth data proved effective in calibrating the experiment sites.

7. Because reflections constrained location depths to the stimulated, producing interval of the Austin chalk, we fixed location depth and were then able to locate 96 (20% of total) Cook's Point and 490 (60% of total) Matcek events.

8. At both sites, elongated seismic zones extend up to 1 km and trend N60°E from the stimulation wells, parallel to the expected fracture direction based on the regional geology. However, the widths of the seismic zones are quite different, measuring over 100 m at Cook's

Point and narrowing to 30 m at the Matcek site.

9. Oil production was much more successful following stimulation at Cook's Point, where we observe the wider seismic zone. Perhaps the microseismicity indicates a higher density of fractures and that a larger volume of the reservoir was affected by the stimulation.

Acknowledgments

Tom Gardner and Mike Miller of Exxon USA were tremendously helpful in coordinating all phases of this work. We also thank Michael Fehler, James Albright, Robert Hanold and Nick Valenti for their efforts in initiating this project. Leigh House, Grady Rhodes and Rod Flores assisted with the data acquisition. Help from Butch Humphries, Cab Craig and Chris Ruusaart with field operations is gratefully acknowledged. Additional thanks go to employees of BJ Services, Bryan, and Magnum Wireline, Giddings for their cooperation. Comments from two anonymous reviewers helped improve the manuscript. This project was supported by the Department of Energy, Oil Recovery and Technology Partnership.

References

- Albright, J. N. and Pearson, C.F., 1982. Acoustic emissions as a tool for hydraulic fracture location: experience at Fenton Hill Hot Dry Rock site. *SPE Journal*, 22: 523-530.
- Baria, R. and Green, A., 1986. Seismicity induced during a viscous stimulation at the Camborne School of Mines Hot Dry Rock geothermal Energy project in Cornwall, England. In: *Proc. Progress in Acoustic Emission III*, Japanese Soc. of NDI: 407-429.
- Batchelor, A. S., Baria, R. and Hearn, K., 1983. Monitoring the effects of hydraulic stimulation by microseismic event location, a case study. *Paper SPE*: 12109.
- Block, L., Fehler, M.C, Cheng, C.H. and Phillips W.S., 1994. Seismic imaging using microearthquakes induced by hydraulic fracturing. *Geophysics*, 59: 102-112.
- Cornet, F.H. and Scotti, O., 1993. Analysis of induced seismicity for fault zone identification. *Int. J. Rock Mech. Min. Sci. & Geomech. Abstr.*, 30: 789-795.
- Fehler, M.C. and Pearson, C.F., 1984. Cross-hole seismic surveys: Application for studying subsurface fracture systems at a hot-dry-rock geothermal site. *Geophysics*, 49: 37-45.
- Fehler, M.C. and Phillips, W.S., 1991. Simultaneous inversion for Q and source parameters of microearthquakes accompanying hydraulic fracturing in granitic rock. *Bull. Seism. Soc. Am.*, 81: 553-575.

- Fehler, M.C., House, L.S. and Kaieda, H., 1987. Determining planes along which earthquakes occur: Method and application to earthquakes accompanying hydraulic fracturing. *J. Geophys. Res.*, 92: 9407-9414.
- Flinn, E. A., 1965. Signal analysis using rectilinearity and direction of particle motion. *Proc. IEEE*, 53: 1725-1743.
- House, L. S., 1987. Locating microearthquakes induced by hydraulic fracturing in crystalline rock. *Geophys. Res. Lett.*, 14: 919-921.
- Keck, R.G. and Withers, R.J., 1994. A field demonstration of hydraulic fracturing for solids waste injection with real-time passive seismic monitoring. paper SPE: 28495.
- Lee, W.H.K., Tottingham, D.M. and Ellis, J.O., 1989. Design and implementation of a PC-based seismic data acquisition, processing and analysis system. In: W.H.K. Lee (Editor), *Toolbox for seismic data acquisition, processing and analysis. IASPEI Software Library*, 1: 21-46.
- Mueller, M. C., 1992. Using shear waves to predict lateral variability in vertical fracture intensity. *The Leading Edge*, 11: 29-35.
- Niitsuma, H., Chubachi, N. and Takanohashi, M., 1987. Acoustic emission analysis of a geothermal reservoir and its application to reservoir control. *Geothermics*, 16: 47-60.
- Pavlis, G.L. and Booker, J.R., 1980. The mixed discrete-continuous inverse problem: Application to the simultaneous determination of earthquake hypocenters and velocity structure. *J. Geophys. Res.*,

85: 4801-4810.

Pearson, C., 1981. The relationship between microseismicity and high pore pressure during hydraulic stimulation experiments in low permeability granite rocks. *J. Geophys. Res.*, 86: 7855-7864.

Phillips, W.S., House, L.S. and Fehler, M.C., 1997 in review. Detailed joint structure in a geothermal reservoir from studies of induced microearthquake clusters. *J. Geophys. Res.*

Phillips, W.S., Rutledge, J.T., Fairbanks, T.D., Gardner, T.L., Miller, M.E., and Schuessler, B.K., 1996. Reservoir fracture mapping using microearthquakes: Austin chalk, Giddings field, TX and 76 Field, Clinton Co., KY. Paper SPE: 36651.

Randall, G.E., 1994. Efficient calculation of complete differential seismograms for laterally homogeneous earth models. *Geophys. J. Int.*, 118: 245-254.

Roff, A., Phillips, W.S. and Brown, D.W., 1996. Joint structures determined by clustering microearthquakes using waveform amplitude ratios. *Int. J. Rock Mech. Min. Sci. & Geomech. Abstr.*, 33: 627-639.

Vidale, J. E., 1986. Complex polarization analysis of particle motion. *Bull. Seism. Soc. Am.*, 76: 1393-1405.

Vinegar, H. J., Wills, P.B., DeMartini, D.C., Shylapobersky, J., Deeg, W.F., Adair, R.G., Woerpel, J.C., Fix, J.E. and Sorrells, G.G., 1991. Active and passive seismic imaging of a hydraulic fracture in diatomite. Paper SPE: 22756.

Warpinski, N.R., Wright, T.B., Uhl, J.E., Engler, B.P., Drozda, P.M., Peterson, R.E. and Branagan, P.T., 1996. Microseismic monitoring of the B-sand hydraulic fracture experiment at the DOE/GRI Multi-Site project, Paper SPE: 36450.

Figures

Figure 1. Microseismic experiment sites at Cook's Point and Matcek Ranch in the Giddings field, Texas. Map and east-west cross-section views are shown. Monitor and injection wells are indicated with well names in parenthesis. The known fracture system trends N60°E in this area. Seismically significant layers are noted in the cross-section views, along with P-wave velocities from sonic logs. The Ector member of the Austin chalk is highlighted, this is the oil-producing layer in this area of the Giddings field. Depths are measured from the surface and are exaggerated by a factor of 2.

Figure 2. Well-head pressure and the number of identifiable microearthquakes per 10 minute interval versus local time for stimulations at the Matcek (top) and Cook's Point (bottom) sites.

Figure 3. Seismograms recorded for a microearthquake (event B1) at Cook's Point. Vertical, radial and transverse components of ground-motion velocity are shown. The fourth trace is a product of vertical and radial components, indicating the quadrant of motion in the vertical-radial plane. Direct P, SV, and SH arrivals are marked, along with an SV-to-SV reflection from the Eagleford-Buda interface below the Austin chalk. The reference time was chosen arbitrarily. Ground motion scales are the same for the three components.

Figure 4. Displacement spectra for 70-ms P, SV and noise windows from the vertical-component seismogram shown in Figure 4 (event B1). A 3-point smoother has been applied to the spectra.

Figure 5. Synthetic, double-couple, point source seismograms

calculated for the Cook's Point structure using velocities found during calibration. A Q of 50 was assigned to all layers. Source depth was 2130 m and distance was 325 m. A source orientation of strike $N80^{\circ}W$, dip 40° and rake -70° was chosen to mimic the seismogram shown in Figure 4. Vertical, radial, transverse and vertical-radial product traces are shown.

Figure 6. Shear-wave splitting (SV-SH) versus SV-P times recorded by the Matcek 3, Matcek 4 and Cook's Point geophones.

Figure 7. Shear-wave splitting (SV-SH), after correcting for travel distance, versus P-wave, particle-motion azimuth recorded by the Matcek 3, Matcek 4 and Cook's Point geophones. We corrected for distance using linear fits to the dominant trends in the data from each geophone shown in Figure 6.

Figure 8. Seismograms recorded for the perforation shot at Cook's Point. Vertical, radial and transverse components of ground-motion velocity are shown along with the vertical-radial product trace, indicating the quadrant of motion in the vertical-radial plane. Direct P and SH phases are marked, along with P-to-P and P-to-SV reflections off the Eagleford-Buda interface below the Austin chalk. The reference time was chosen arbitrarily. Ground motion scales are the same for the three components.

Figure 9. P-wave, hodogram inclination versus SV-P time recorded by the Matcek 3, Matcek 4 and Cook's Point geophones. Filled regions represent the possible range of incidence angles for events located in the Ector member of the Austin chalk. The Matcek-3 geophone was deployed within the Ector layer, the Matcek-4 and Cook's

Point geophones were deployed above it. Inclinations greater than 90° represent downgoing raypaths at the Matcek-3 geophone.

Figure 10. Locations obtained during calibration using high-quality microearthquake data collected at the Matcek site: map view (top) and east-west cross section (bottom). Projections of the standard error ellipsoids are indicated for selected events. The injection point and geophone positions are shown in the cross section (solid circles). The Ector member of the Austin chalk is shaded. Depth is exaggerated by a factor of 2.

Figure 11. Locations of high-quality Cook's Point microearthquakes that generated a reflected arrival, using calibration velocities from the Matcek site: map view (top) and east-west cross section (bottom). Projections of the standard error ellipsoids are indicated for selected events. The injection point and geophone position are shown in the cross section (solid circles). The Ector member of the Austin chalk is shaded. Depth is exaggerated by a factor of 2.

Figure 12. Microearthquake locations obtained by fixing depth to the stimulated interval at the Matcek (top) and Cook's Point (bottom) sites. Map scales are identical. Reference positions are the Matcek 4 and CPU 1-2 monitor wells. Standard error ellipses are shown for selected events.

Figure 13. Average daily oil rate over monthly intervals before and after hydraulic stimulation in wells CPU 2-2 (Cook's Point, triangles) and Matcek 1 (squares).

Figure 14. Microearthquake locations at the Matcek site using data

from only the Matcek 4 (top) and Matcek 3 (bottom) geophones, fixing depth to the injection interval. The reference position is the Matcek 4 well.

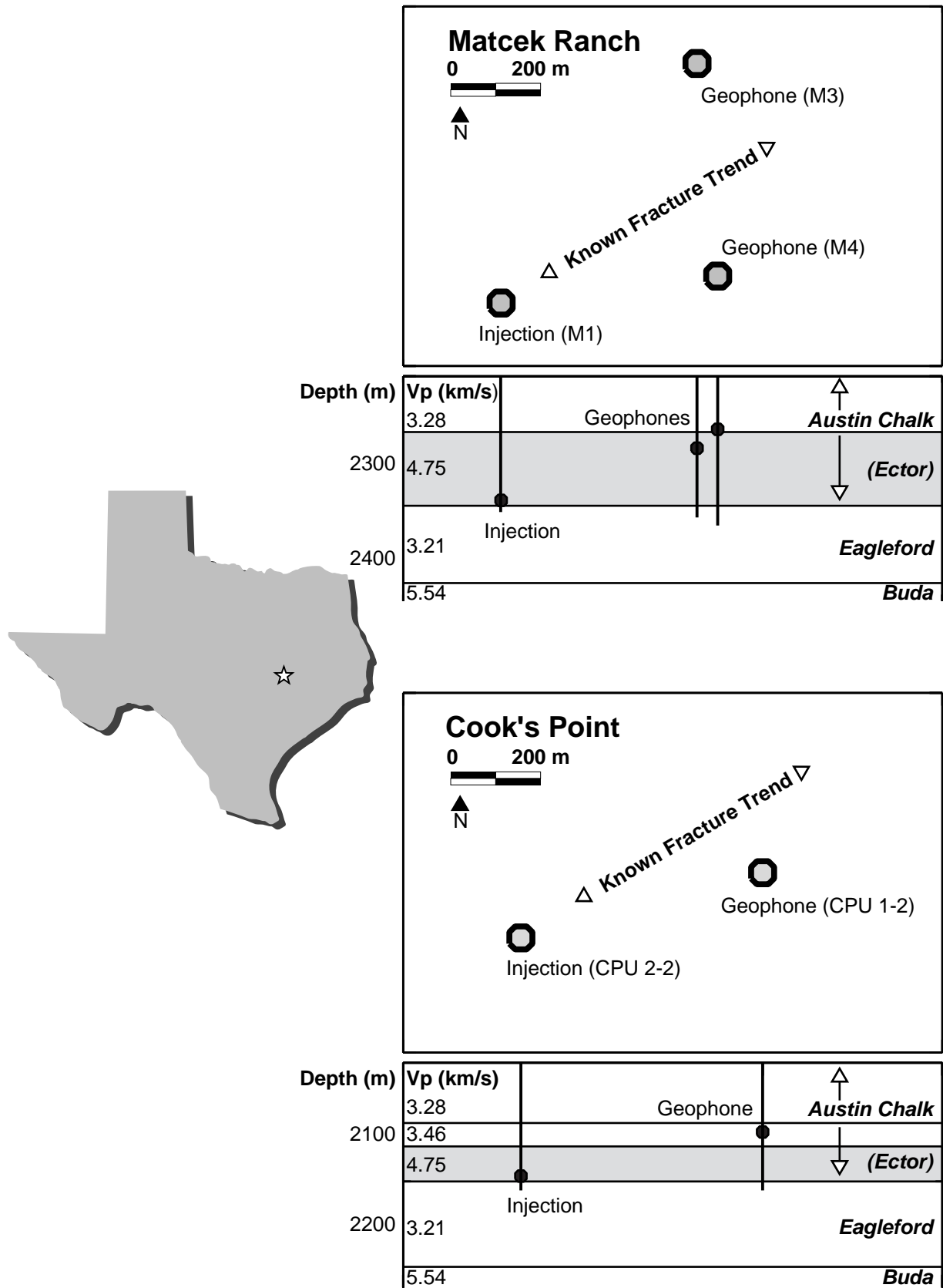


Figure 1

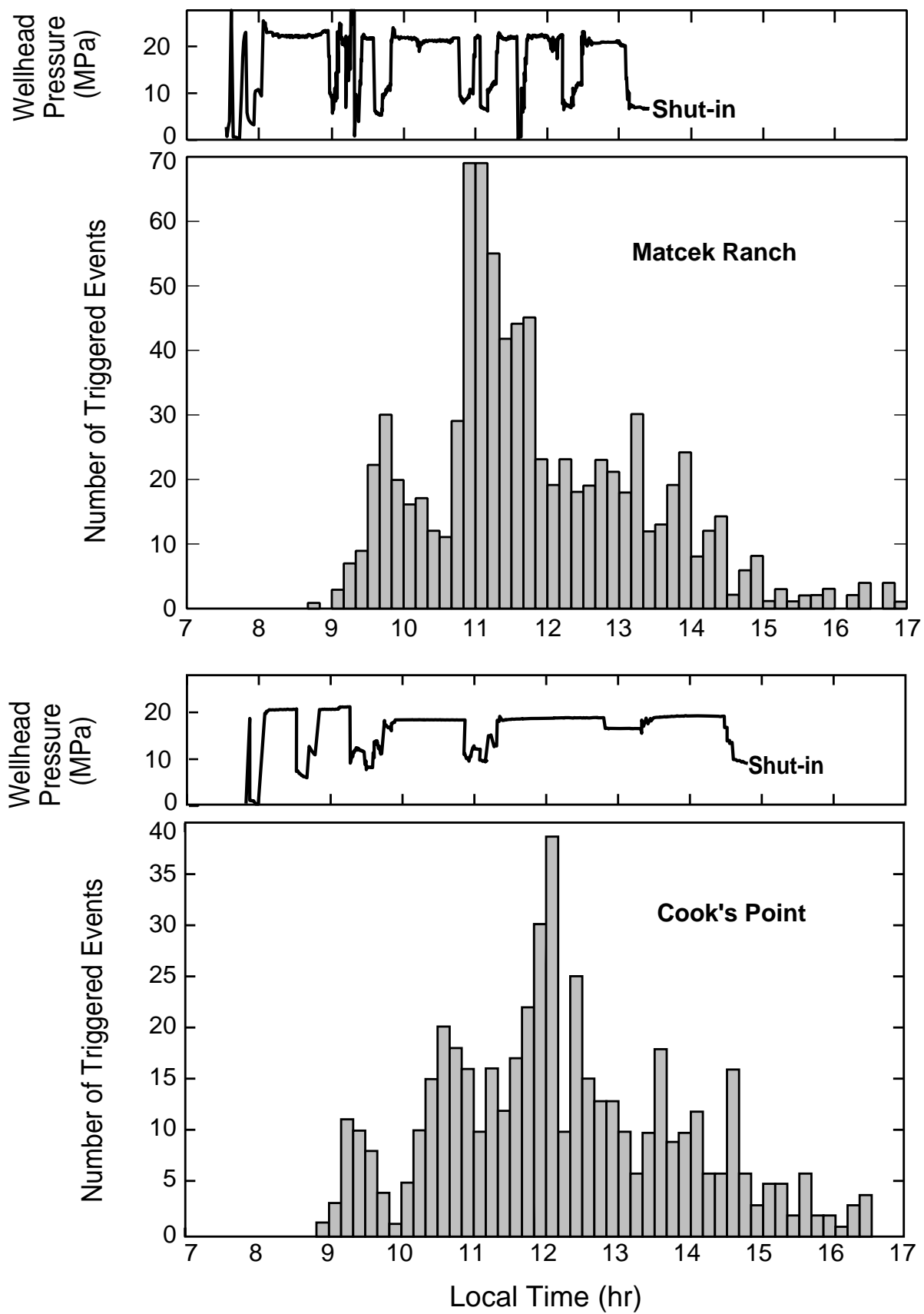


Figure 2

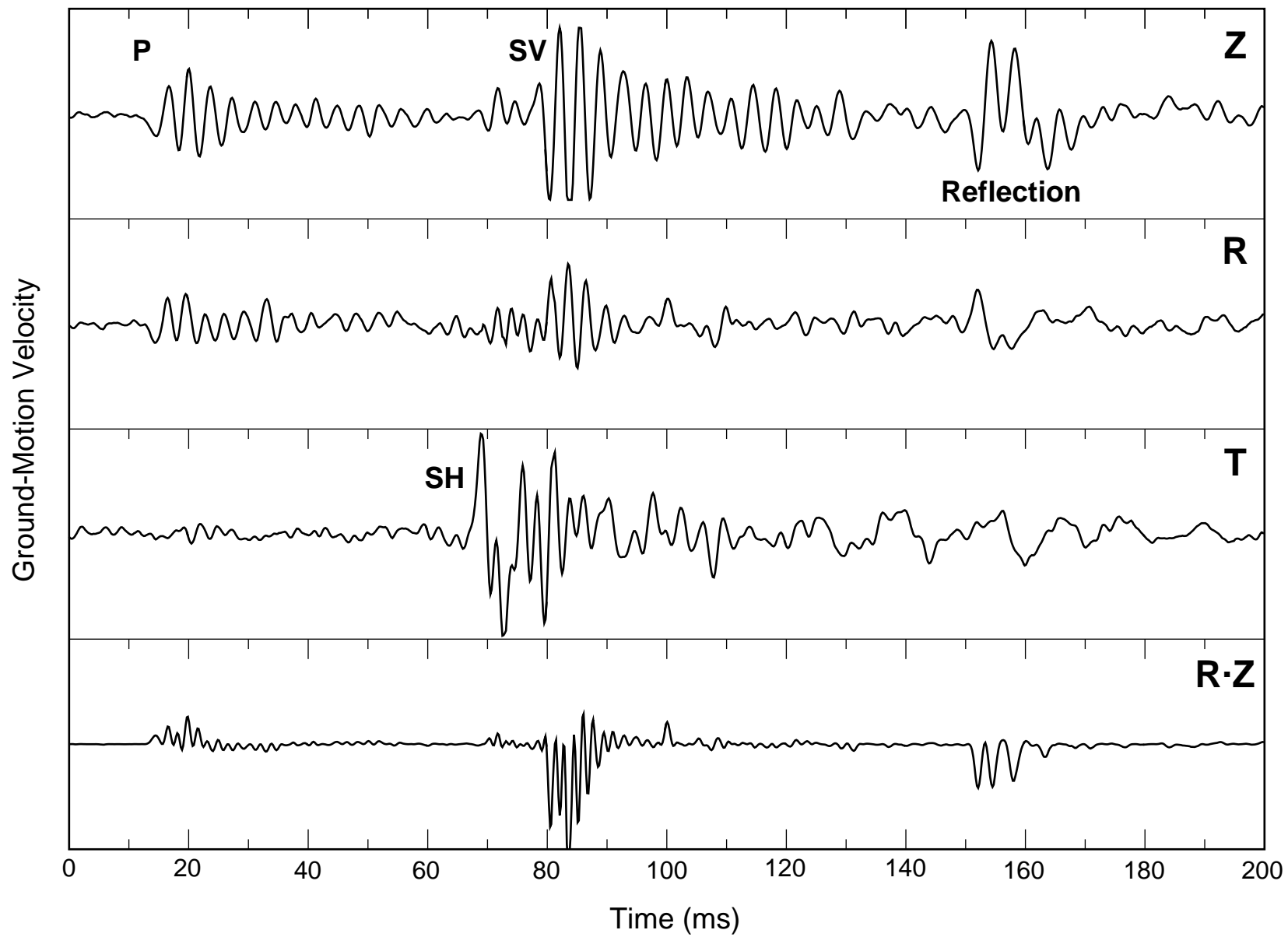


Figure 3

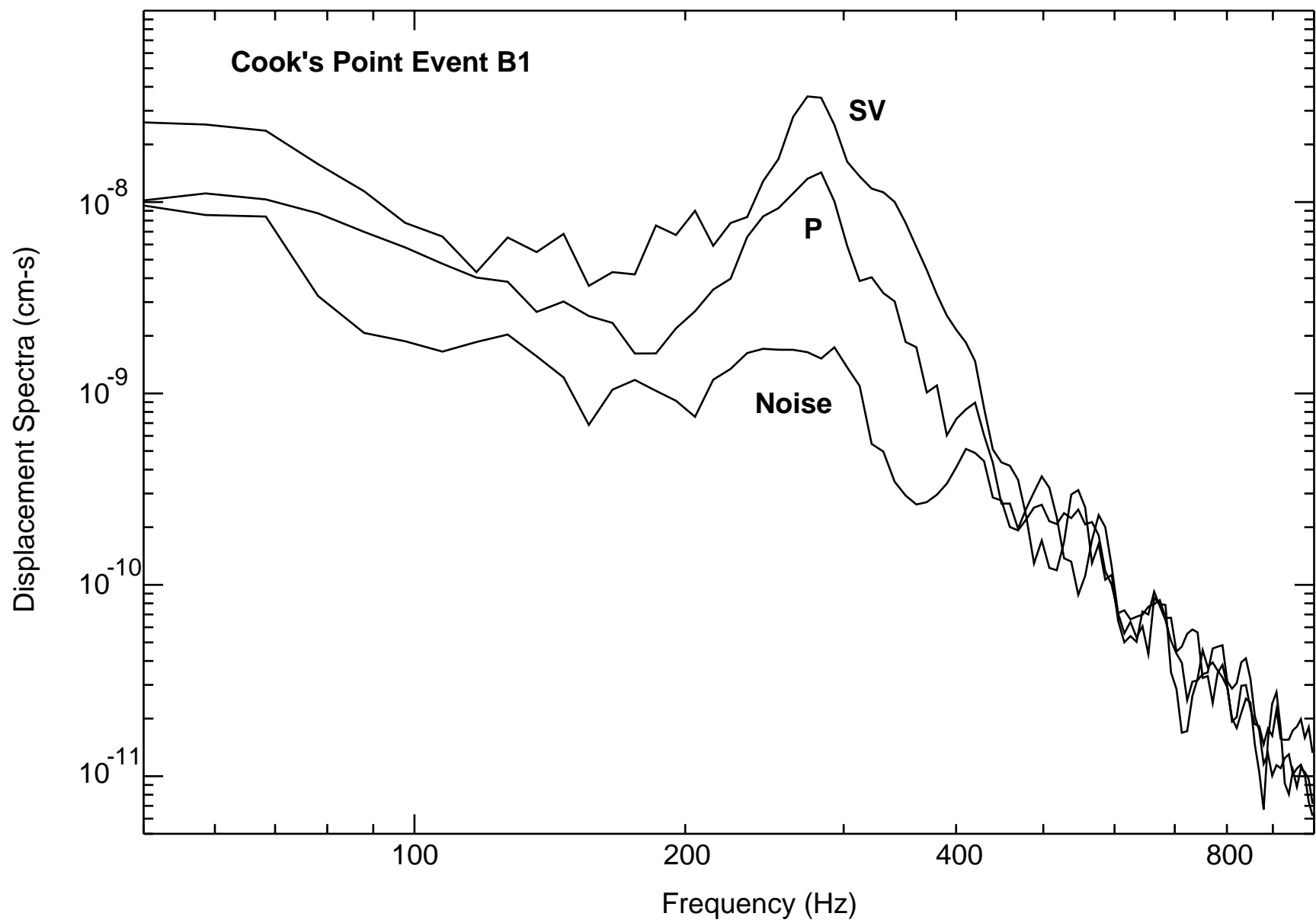


Figure 4

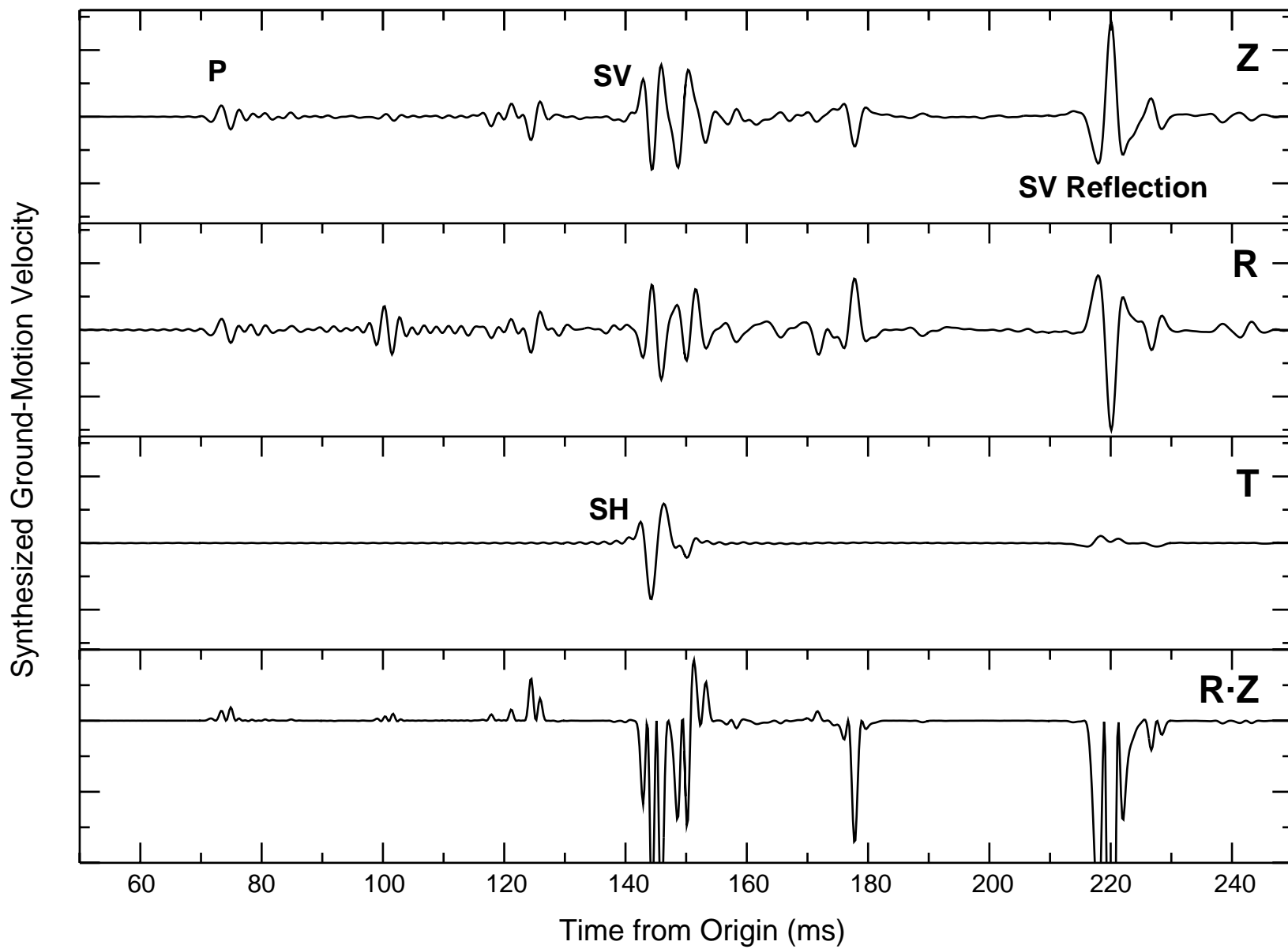


Figure 5

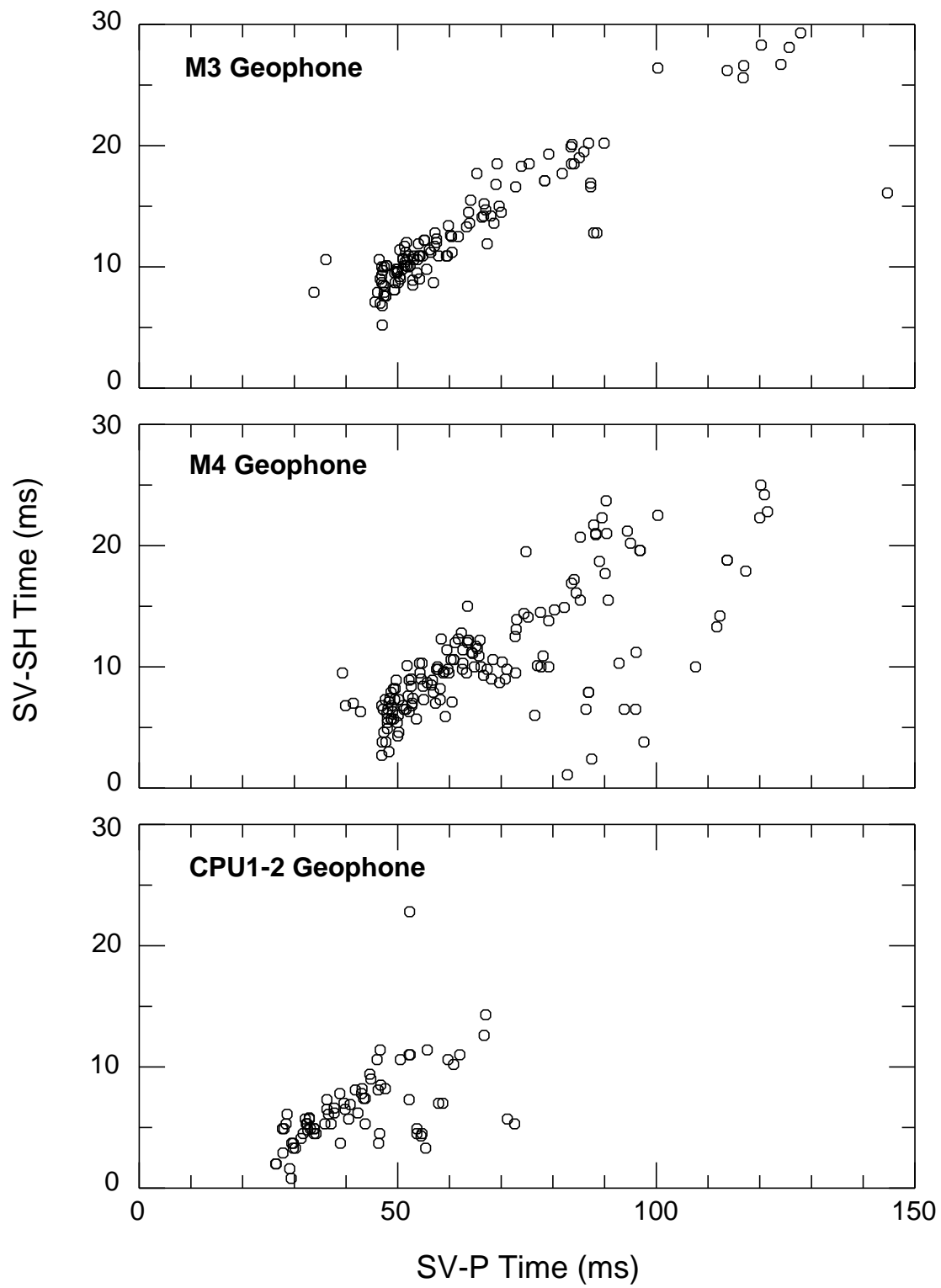


Figure 6

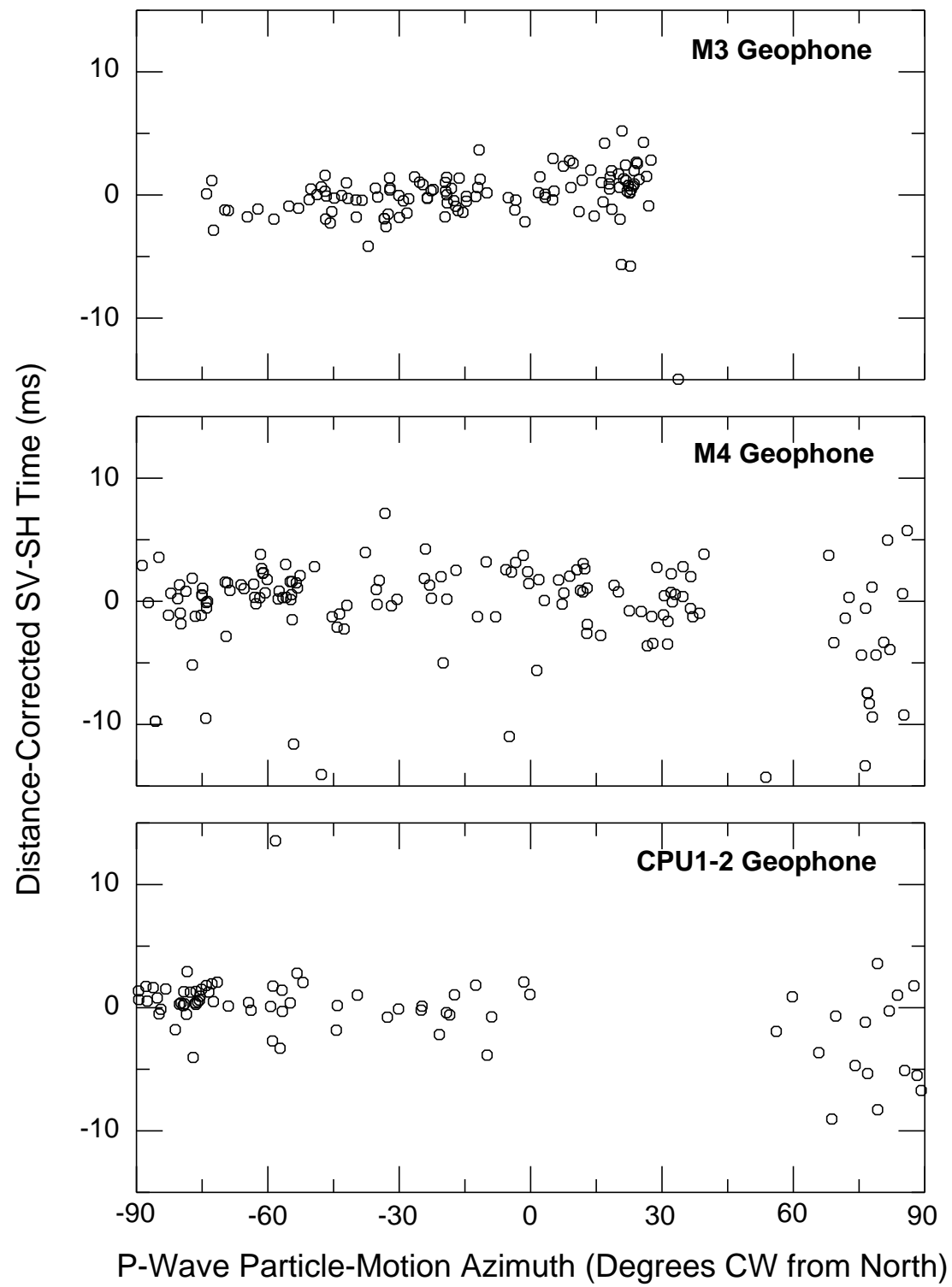


Figure 7

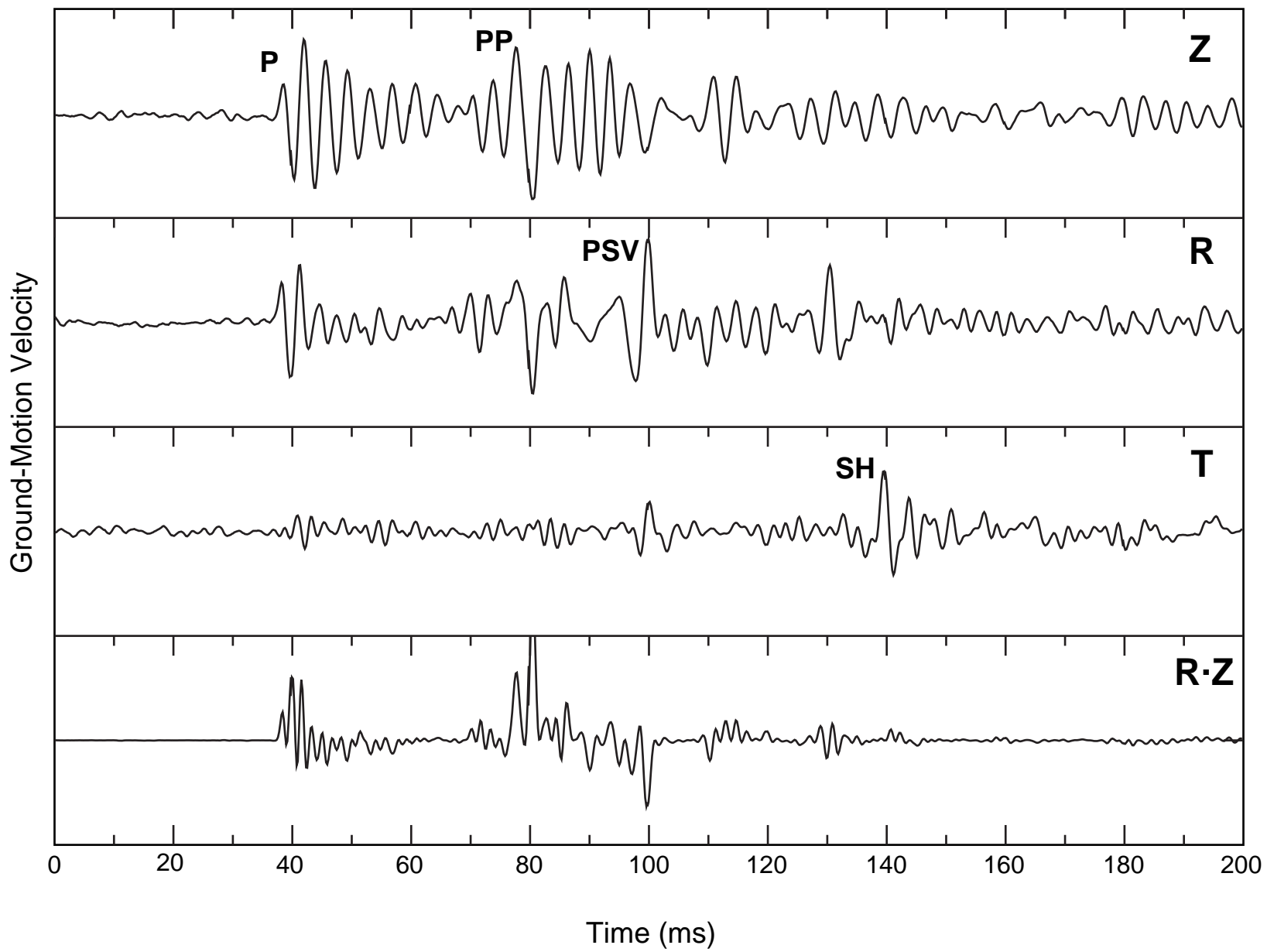


Figure 8

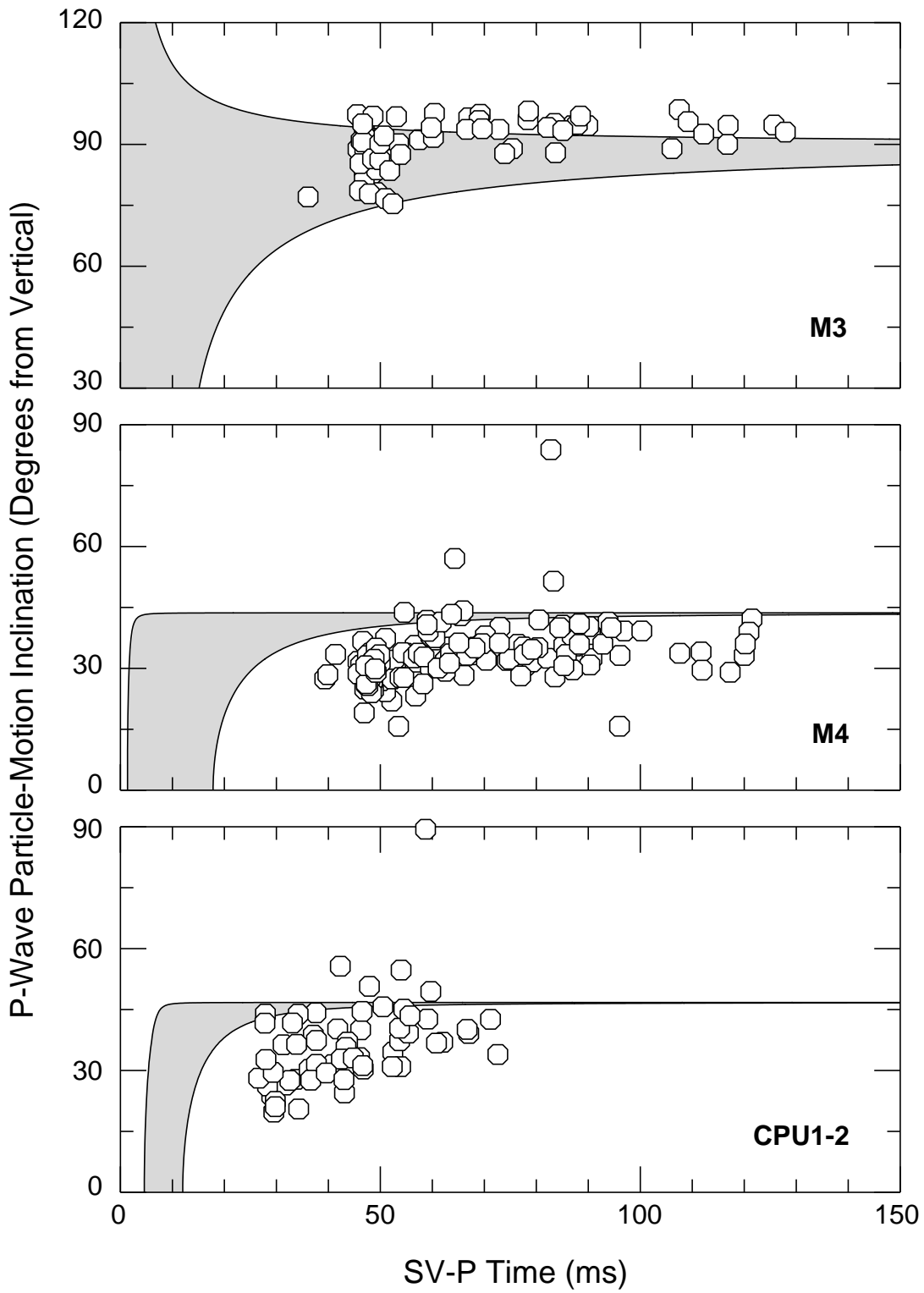


Figure 9

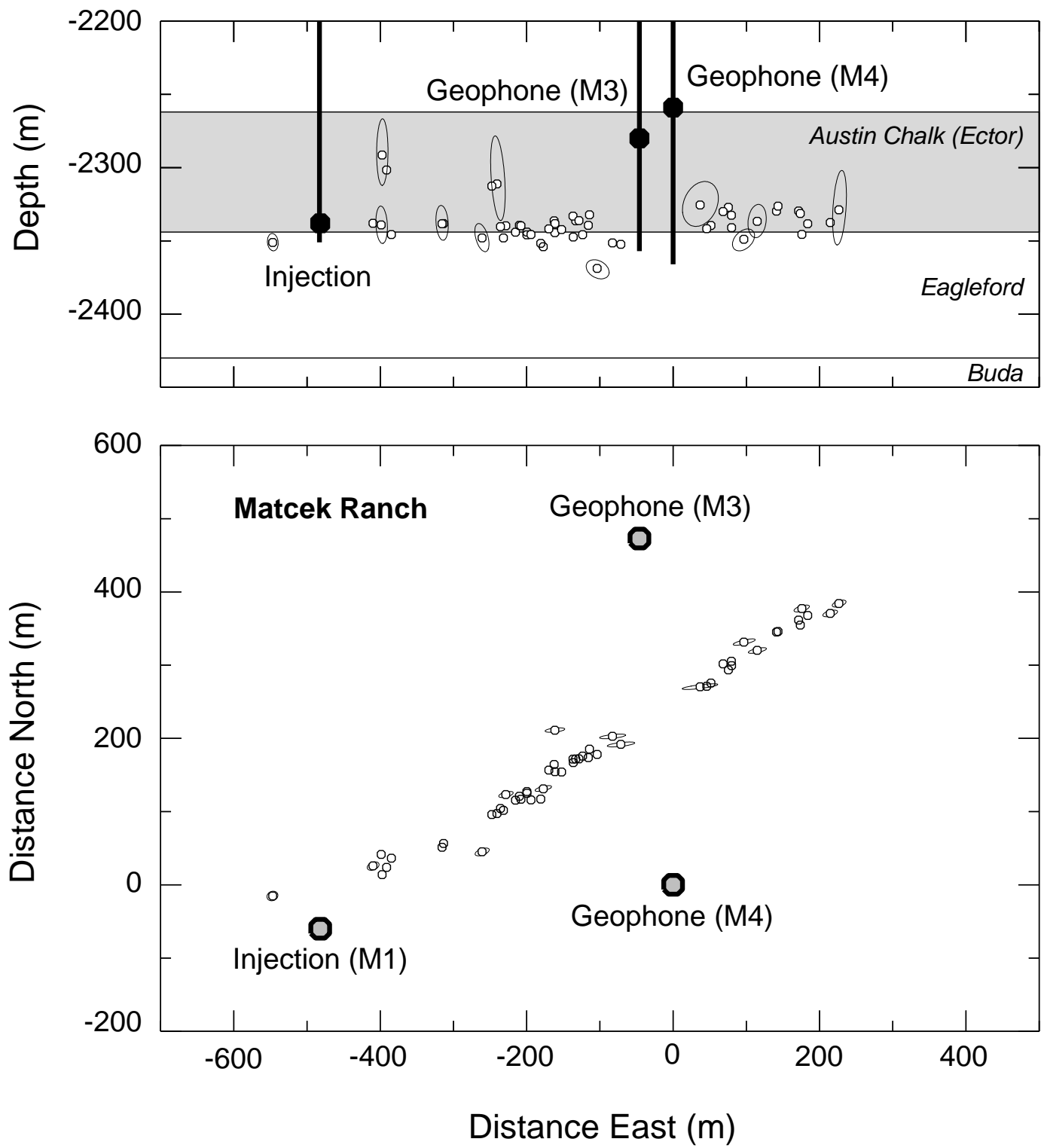


Figure 10

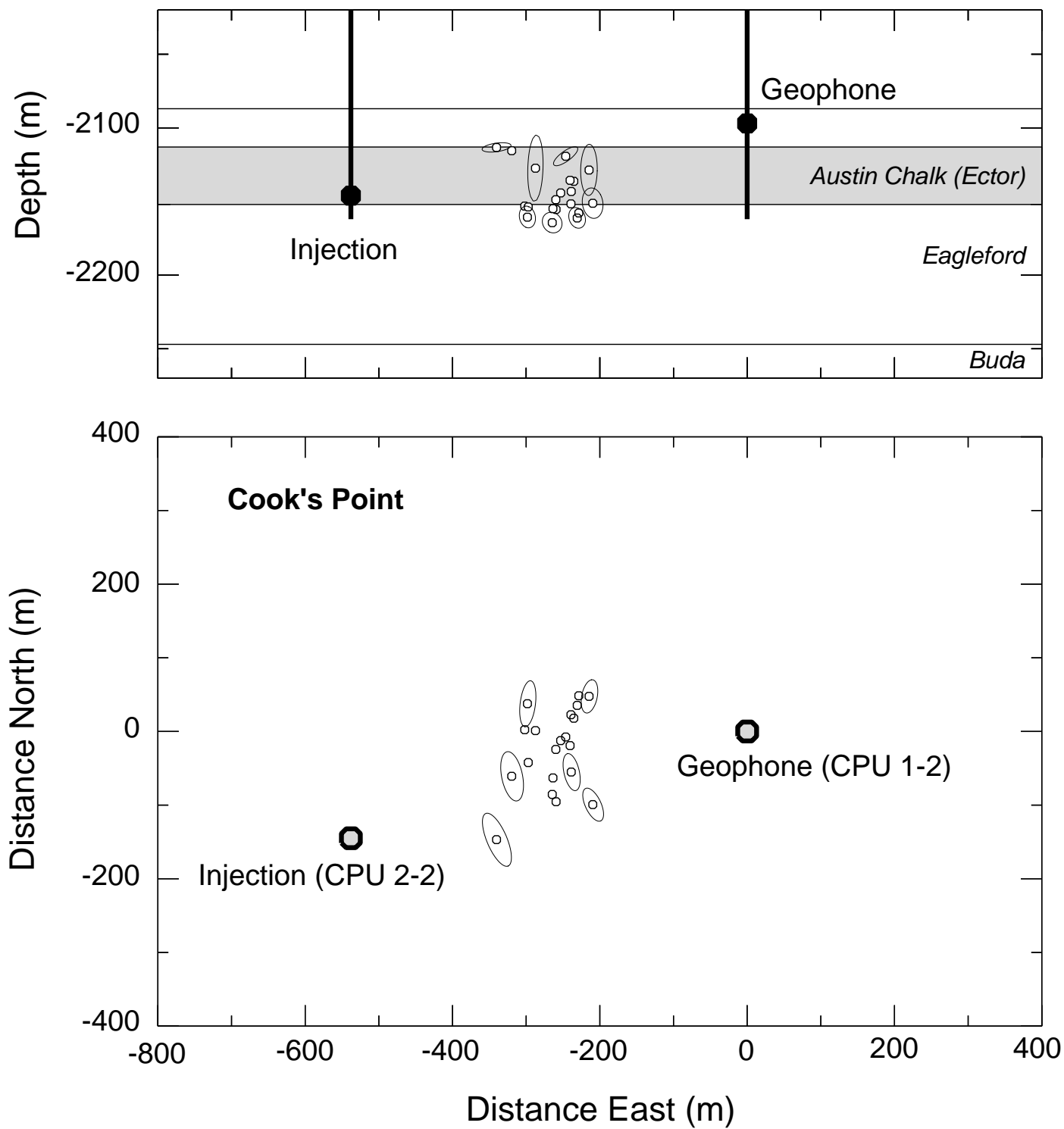


Figure 11

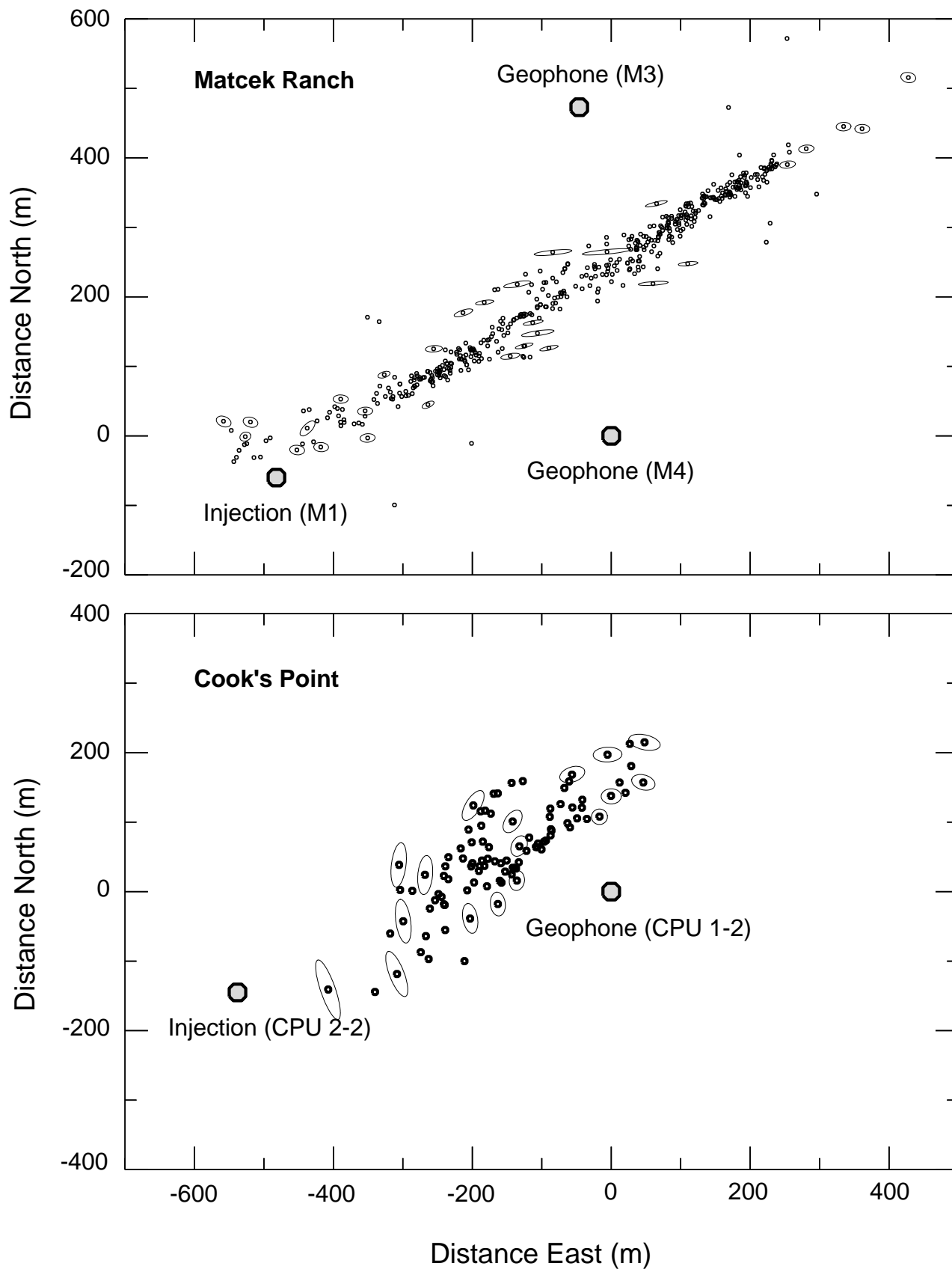


Figure 12

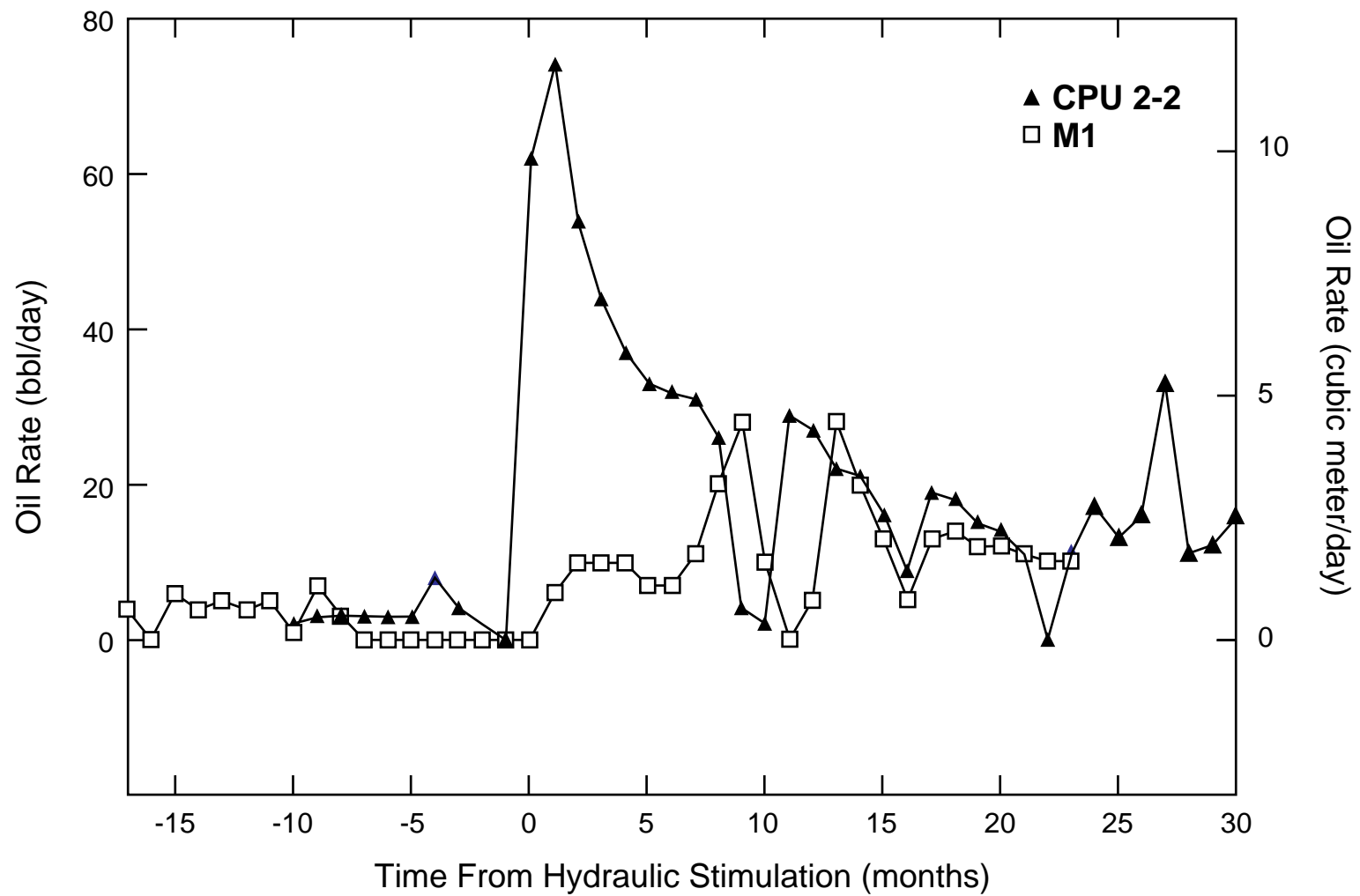


Figure 13

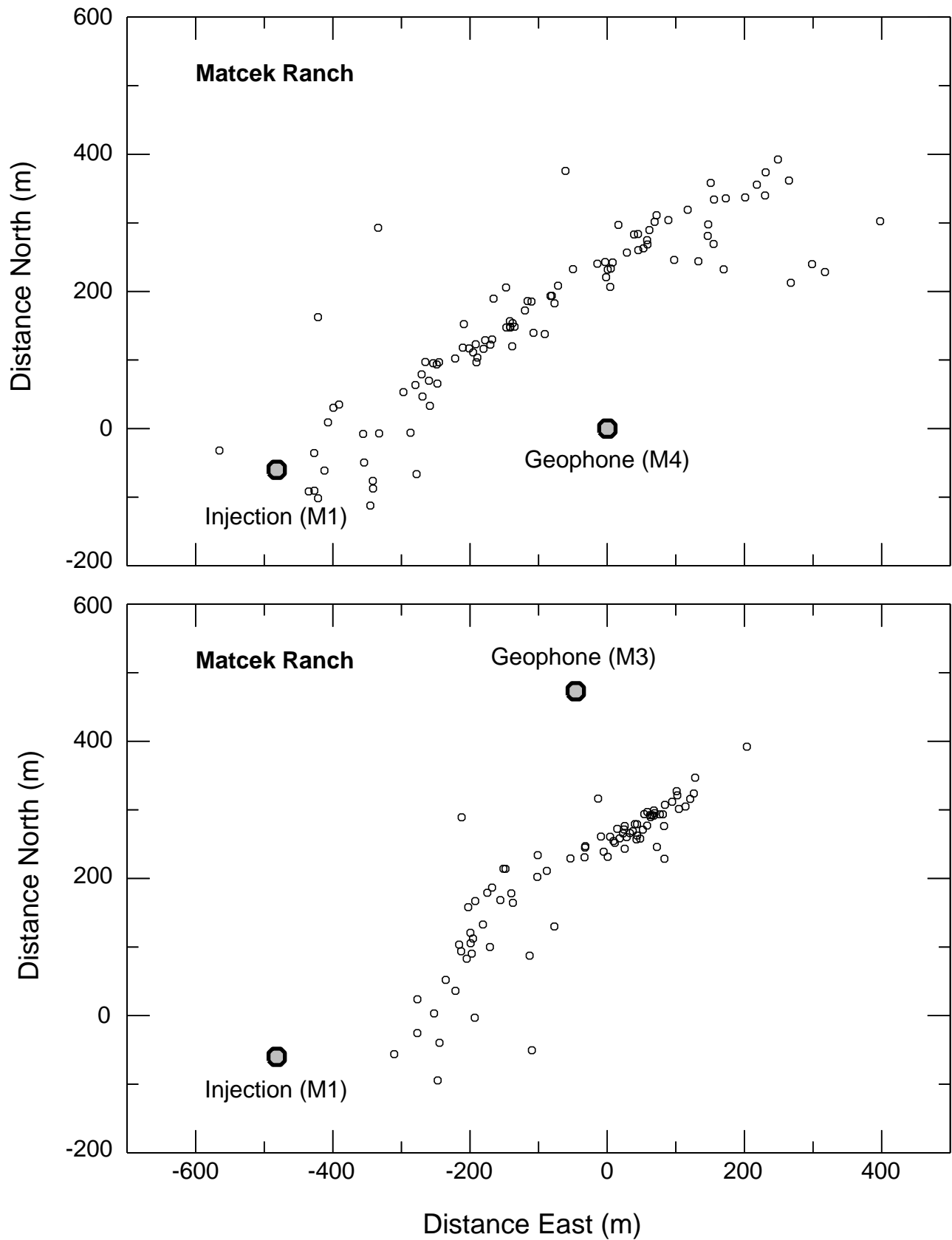


Figure 14